

Flexible solid-state Ge – LiCoO₂ battery: From materials to device application

Eliana M. F. Vieira^{1*}, Joao F. Ribeiro¹, Rui Sousa², Anabela G. Rolo³, Manuela M. Silva⁴, Luis M. Goncalves¹

¹CMEMS - UMINHO, University of Minho, Campus Azurem, Guimaraes, 4804 - 533, Portugal

²DEI, University of Minho, Campus Azurem, Guimaraes, 4804 -1533, Portugal

³Physics Center and Physics Department, University of Minho, Campus Gualtar, Braga, 4710- 057, Portugal

⁴Chemistry Center, University of Minho, Campus Gualtar, Braga, 4710 - 057, Portugal

*Corresponding author: Tel: (+351)-253-510190; E-mail: evieira@dei.uminho.pt

Received: 30 September 2016, Revised: 09 December 2016 and Accepted: 23 January 2017

DOI: 10.5185/amlett.2017.1429

www.vbripress.com/aml

Abstract

Design and fabrication of reliable materials with high capacity, cycling stability and good adhesion properties for flexible microbatteries remains a challenge. A 2 μm thick flexible solid-state Ge-LiCoO₂ battery was fabricated and the structure, composition, thermal, optical, electrical, and electrochemical properties of the materials that determine and influence its electrochemical potential were investigated. RF-sputtered lithium cobalt oxide (LiCoO₂) cathode and lithium phosphorus oxynitride (LiPON) electrolyte films were fabricated at 120 W and 100 W of power, respectively. A \sim 300 nm thick Ge anode was deposited by e-beam. The full-battery was fabricated using conventional and low-cost PVD processes. X-ray diffraction (XRD) and Raman spectroscopy confirms the hexagonal R $\bar{3}m$ phase of annealed LiCoO₂. Differential scanning calorimetry (DSC) technique was applied to investigate the thermal behaviour of the LiPON film with a moderate electrical resistivity of 10⁸ Ωcm and high optical transmission (> 75%) in the UV-Visible range. Bending experiments were also performed to evaluate thin-films adhesion and stability. Scanning electron microscopy (SEM) technique was used to evaluate the morphology of films surface and the layered structure of the full-battery. This detailed experimental study allows us to understand the discharge behavior of the fabricated Li-ion battery. Copyright © 2017 VBRI Press.

Keywords: Flexible, thin-film, li-ion battery, bending, energy storage.

Introduction

Li-ion battery technology is already in use for low power applications such as consumer electronics and power tools. Extensive research has projected the application of this technology toward renewable energy sources (such as, solar cells and windmills) [1] [2], human and animals [3]. However, the battery safety, lifetime and generated power is still a concern. Furthermore, for these kind of applications, when thin-film micro-architecture battery is directly engineered and fabricated as a part of an integrated circuit (taking in account compatible manufacturing processes), the battery implementation process is easier. Additionally, if the batteries are flexible, lightweight and thin, this technology could be expanded to more specific applications (e. g. implantable medical devices).

Electrochemical energy storage devices are very complex. They are multicomponent systems that incorporate widely dissimilar phases in physical and electrical contact [4]. Operation of a rechargeable battery relies critically on electron and ionic transfer across the solid/solid interfaces (for thin-film electrolyte) and

solid/liquid interfaces (for liquid electrolyte) and within each of the constituent elements. Moreover, repeatedly charging/discharging processes of the battery induces microstructural evolutions not only at the electrodes/electrolyte interfaces as well as within the active materials due to the electronic conduction and ionic migration [4]. The main challenge in the design of rechargeable thin-film Li-ion battery is to ensure that the electrodes keep their mechanical integrity over many charge/discharge cycles. The diffusion of lithium ions, the reaction rate at the cathode/electrolyte interface, and the adhesion between the materials [5] of the multilayer system are critical for the performance and durability of the desired batteries.

The main active materials in the battery is the cathode, the anode and the electrolyte. For Li-ion batteries and among all valuable cathode materials studied, lithium cobalt oxide (LiCoO₂) is an attractive cathode material due to high theoretical specific capacity of 247 mAhg⁻¹, high theoretical volumetric capacity of 1363 mAhcm⁻³, low self-discharge, high discharge voltage (4.1 V vs Li⁺/Li), and good cycling performance [6] [7]. LiCoO₂ crystallographic structure is usually separated by the so

called low temperature LiCoO₂ (LT-LiCoO₂) that has the lattice of the cubic spinel (space group Fd3m) and high temperature LiCoO₂ (HT-LiCoO₂) that has a hexagonal lattice (space group R $\bar{3}$ m) [8]. HT-LiCoO₂ is the most suitable for application in lithium microbatteries [9], [10]. J. B. Bates, *et al.* [11] go further and explain that the crystallization of LiCoO₂ films should privilege the plane (101), which provides a structure perpendicular to the substrate and improves lithium cycling. To achieve the desired crystallographic structure, an annealing at 700 °C for 1 hour is usually needed, which is impracticable in plastic/polymeric substrates.

For high performance electrolyte, a high ionic conductivity (to allow fast Li ions movement and therefore, minimal internal resistance), negligible electrical conductivity (to prevent the self-discharge of the cell), chemical compatibility with the electrode materials, and electrochemical stability at high voltage window and in a wide range of temperature [12–14] are needed. Moreover, the use of a solid-state electrolyte (e.g. lithium phosphorus oxynitride (LiPON)) eliminates leaking or explosion risk (present with liquid electrolytes) and offers stability and good endurance to adverse environmental conditions [15]. LiPON exhibits electrochemical stability window up to 5.5 V vs Li⁺/Li [16], which could be combined with high voltage cathodes [17], moderate ionic conductivity of 10⁻⁶ Scm⁻¹ at room-temperature [12] and high electronic resistivity of ~10¹⁴ Ωcm [18]. Metallic lithium is the anode material that presents higher specific power, but presents many problems due to the dendrites formation of Li metal, leading to a short-circuits and undesirable thermal reactions on the cathode and consequently battery burning [19]. For this work, a germanium (Ge) material was used as anode of the solid-state li-ion battery. Ge shows a high theoretical gravimetric capacity of 1568 mAhg⁻¹ and the ability to alloy with 4.4 Li atoms per Ge atom [20], fast Li ion-transport kinetics (400 times higher than Si at room temperature) and lower volume change during cycling mechanisms, which can support high charge/discharge cycles [21] [22]. Ge can store ≈ 8 times more Li atoms than LiCoO₂ (0.5 Li atoms per CoO₂ and 4.4 Li atoms per Ge) [11] [20]. Besides these materials, carbon nanotubes (CNTs), graphene and low-dimensional nanostructured materials are other examples of light-weight, robust and flexible materials that have been reported in recent years, to achieve high area and volumetric capacities in Li-ion batteries [23]. To overcome strain effects from volume change after lithiation, and extend the battery cyclic stability, S. Fang *et al.* [24] reported a hybrid anode for Li-ion batteries constructed by Ge nanoparticles – graphene - carbon nanotube that delivers a high-energy capacity up to 863.8 mAh/g, at a current density of 100 mA/g after 100 cycles. In turn, a 3D vanadium pentoxide (V₂O₅)/reduced graphene oxide (RGO)/carbon nanotube structure reported by the K. Palanisamy *et al.* [25] arises as a promising cathode architecture for high – performance Li-ion batteries due to the observed high capacity of 220 mAh/g at 1C after 80 cycles. This network structure creates channels for effective Li ion

transport and increase surface Li⁺ storage. An original concept of battery architecture was demonstrated by LG Chem. Ltd [26], a cable – type Li-ion battery characterized by a hollow spiral nickel/tin-coated copper wires (anode), a lithium cobalt oxide (LiCoO₂) cathode composite, and a modified polyethylene terephthalate (PET) nanowoven separator membrane. A potential plateau of 3.5 V and an initial specific capacity of 1 mAh/cm were observed. This kind of battery can be adapted to fit nearly anywhere, facilitating the integration in practical wearable electronics. However, further improvement is needed relatively to the capacity retention results with cycling. Although it has been established that the active materials properties are responsible for battery performance, the correlation of these with the charging/discharging of the full battery are not well discussed [27].

In this work, the structure, composition, thermal, optical, electric, and electrochemical properties of the cathode and electrolyte active materials are investigated and correlated with the electrochemical potential of the full Li-ion battery. A flexible solid-state Li-ion battery of LiCoO₂/LiPON/Ge (cathode/electrolyte/anode) was developed by simplified, low-cost and micro-electromechanical systems (MEMS) technology compatibility, which is essential for industry fabrication requirements. Kapton® sheets of 127 μm thick [28] were used as battery substrate because holds temperatures up to 400 °C and provides flexibility to the battery. A silicon nitride (Si₃N₄) barrier layer was deposited on top of the Kapton® to prevent the lithium ions migration to the substrate during the charge/discharge cycles. Prior the Pt cathode current collector, a Ti layer was deposited to improve the adhesion between the Si₃N₄ and Pt layers. Among the cathode and electrolyte properties, bending experiments were performed to evaluate the adhesion and stability of the battery base structure (kapton/Si₃N₄/Ti/Pt) before the active materials deposition. The Si₃N₄ barrier layer electrical and optical properties were investigated. We have made use of a wide set of characterization techniques (X-ray diffraction (XRD), Raman spectroscopy, differential scanning calorimetry (DSC), electrical resistivity, optical transmittance, scanning electron microscopy (SEM) and electrochemical tests) to give a detailed study of the battery point of view.

To the best of our knowledge, it is the first work that reports a direct correlation between the properties of isolated thin-film materials and their effect on the electrochemical behaviour of the respectively full battery, when they are coupled together. These findings could help the researchers on this field to optimize the design of future all-solid-state thin-films batteries.

Experimental

Materials

The selected fabrication parameters of each battery layer play a critical role on batteries performance and durability. Each battery film was prepared taking in account the application in flexible microbatteries.

Kapton® 500 HN from DuPont™ (127 μm thick) was used as substrate to provide a flexible structure. This polyimide can support temperatures up to 400 °C [29]. Several films were deposited on the substrate, prior the LiCoO₂ cathode. Si_xN_y film (500 nm thick) was the first deposited layer. This material was used as lithium barrier layer [30], [31], to prevent Li ions diffusion into the substrate. Si_xN_y films were fabricated by RF sputtering at 250 W of power and, with a constant pressure of 6×10^{-3} mbar during deposition. A 2" single-side polished N - type <100> silicon wafer (1 mm thick and resistivity of 0.5-1.0 Ωcm) was used as sputtering target. To evaluate dependence of the deposition gases in Si_xN_y properties, five different samples were prepared, using Ar and N₂ gases (with high purity of 99,9992%), but assuming a total flow of 20 sccm in the vacuum chamber (see **Table I**). The distance from target to samples is 75 mm.

Table I. Deposition conditions and measured composition of RF-sputtered Si_xN_y films.

Material	Gas		Deposition rate (\AA s^{-1})	Temperature (°C)	Composition (EDS technique)
	N ₂ (sccm)	Ar (sccm)			
Si _x N _y	20	0	0.7	79	Si ₃ N _{4,13}
	16	4	0.8	79	Si ₃ N _{3,92}
	13	7	0.8	80	Si ₃ N _{4,02}
	10	10	0.9	79	Si ₃ N _{3,83}
	7	13	1.0	76	Si ₃ N _{3,68}

Table II. Fabrication parameters for the active materials of the Li-ion battery.

Material	Target	Deposition technique	Gas (sccm)			Power (W)	Pressure (mbar)	Thickness (nm)	Temp. (°C)
			Ar	N	O				
LiCoO ₂	LiCoO ₂	RF sputtering	17	-	3	120	6×10^{-3}	500	141
LiPON	Li ₃ PO ₄		-	20	-	100			
Ge	-	E-beam	-	-	-	(7 kV, 40 mA)	-	300	64

The Ti adhesion layer (30 nm thick) plays an important role in improving the Pt adhesion process. Pt (150 nm thick) is the current collector for LiCoO₂. Pt is electrically conductive and avoid unwanted reactions with LiCoO₂ [32], [33]. The LiCoO₂ cathode (1.4 μm) was deposited by RF magnetron sputtering technique, with a 120 W power supply, pressure of 6×10^{-3} mbar and 17/3 sccm of Ar/O₂ flux, respectively. LiCoO₂ film was annealed at 400 °C in an oven for 1 hour, in air conditions. A ramp of 3 °C/min was maintained during the oven heating and cooling to prevent cracks in the film. LiPON electrolyte film was fabricated by RF sputtering of lithium phosphate (Li₃PO₄) target at 100 W of RF power and in 20 sccm of N₂ flux. LiPON thickness was settled to be 1 μm for the battery. The pressure inside the vacuum chamber was set at 6×10^{-3} mbar. The 300 nm Ge anode was deposited by e-beam. The deposition parameters are listed in **Table II**.

Device fabrication

Solid-state Li-ion battery (**Fig. 1**) was fabricated by PVD techniques on top of flexible Kapton® substrate that provides flexibility, good thin-film adhesion and supports all deposited layers. Custom stainless steel shadow masks were specially designed allowing the format required for each battery layer and providing a 1 cm² active area to the battery. RF-sputtered Si₃N₄ layer was first deposited onto de Kapton substrate, with a 250 W of power, pressure of 6×10^{-3} mbar and 7/13 sccm of Ar/N₂ flux. A thin Ti adhesion layer (30 nm thick) was deposited by e-beam technique (7 kV of voltage; 60 mA of current) and Pt cathode current collector (150 nm thick) was deposited by DC- sputtering, with 20 W of power, pressure of 1×10^{-2} mbar and 40 sccm of Ar. Taking in account the battery design, RF-sputtered LiCoO₂ cathode (500 nm thick) was fabricated on top of the Pt layer by deposition and annealing conditions described above, in Battery Materials section. Ti anode current collector (300 nm thick) was deposited by e-beam and before the LiPON electrolyte to prevent undesirable chemical reactions between LiPON and Ti during the deposition of Ti Layer. RF- sputtered LiPON electrolyte film was deposited over the LiCoO₂ cathode by the fabrication parameters mentioned in Battery Materials section. To provide electrodes electrical insulation and battery chemical stability, a barrier composed of Si₃N₄ (20 nm) and LiPO (50 nm) thin films were deposited by RF sputtering, before the Ge anode deposition. This Si₃N₄ layer was deposited with a 100W RF power, lower than the initial Si₃N₄ layer, to prevent damage on the underlying layers due to the temperature increase obtained with higher RF power. The other parameters were kept constant. Moreover, this layer will prevent Li ions to flow between cathode and anode in the limits of the battery, avoiding secondary reactions that could damage the battery. LiPO and Si₃N₄ materials offer the advantage of compatibility with underlying layers. The Ge (300 nm thick) anode was deposited by e-beam, connected by the current collector Ti layer. The fabrication parameters for the active materials are summarized in **Table II**. The design of the fabricated flexible thin-film Li-ion battery is presented on **Fig. 1**. The battery total thickness is about 2.45 μm plus the Kapton® substrate (127 μm thick).

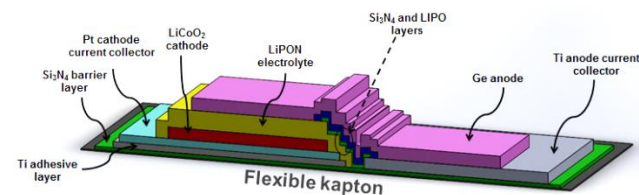


Fig. 1. Design of Li-ion microbattery with materials indication (not on scale for better visualization).

Characterizations

The thickness of the films was measured using a calibrated quartz microbalance inside the vacuum chamber during deposition, and then validated by

profilometry (stylus profilometer Veeco DEKTAK 150), optical transmittance and SEM measurements. A NanoSEM – FEI Nova 200 (FEG/SEM) with an integrated system (EDAX – Pegasus X4M (EDS/EBSD)) of X-ray microanalyses energy dispersive spectroscopy (EDS) was used. Specifically, EDS was used to quantify the element composition of Si_xN_y films. A four-point resistance measurement and surface SEM imaging were performed to evaluate thin-films adhesion and stability after bending experiments. For the optical transmittance, a power of 200 W was applied in the lamp of the spectrophotometer (Oriol 66881). The monochromator (Corner Stone 130 1/8m) made scanning of the wavelength from 300 to 1000 nm and the correspondent light irradiates on Hamamatsu Photodiode Model S1336 – 5BQ, controlled by LabView software. The step used in the wavelength was 1 nm and the mean value of four readings was calculated for the current in photodiode. Films thickness and refractive index were calculated using the method proposed by Swanepoel [34]. Air was taken as reference for transmission measurements. Electrical characterization was performed for Si_xN_y and LiPON films. For the Si_xN_y films, e-beam Al contacts (200 nm thick) were deposited and patterned by photolithography on the top and bottom of the Si_xN_y films, to create a MIM (Metal-Insulator-Metal) structure, on glass substrates. The remainder of Al was removed by wet-etching. A similar MIM structure was fabricated for LiPON films, but to avoid possible reactions at Al/LiPON interfaces, e-beam Ti films (100 nm thick) were deposited between Al and LiPON layers. In this case, the Al and Ti contacts were patterned using typical stainless steel shadow masks on the top and bottom of the LiPON films. We did not use a lithography patterning process to prevent chemical reactions in the LiPON material when in contact with photoresist and etching solutions. Electrical measurements were performed at room-temperature with a picoammeter Keithley 6487, controlled by an own made LabView software. A DC voltage (alternating between positive and negative value in each measurement) was applied in two complementary ways, namely; (i) 0- 10 V with 0.2 V step; and (ii) 0 – 500 V with 2 V step (for Si_xN_y films) and in one procedure between 0 to 10 V with 0.1 V step (for LiPON films), to plot V-I characteristics. The current measurement was taken after 600 milliseconds of voltage application. Electrical resistance was calculated with 1 V applied to the film. Breakdown field was measured dividing the maximum applied voltage without film disruption by the thickness of the film. The thermal behavior of the LiPON films was measured by DSC technique. The DSC scans were performed in argon atmosphere using a Mettler Toledo, DSC821 at a constant heating rate of $10\text{ }^\circ\text{Cmin}^{-1}$ over a temperature range from -60 to $350\text{ }^\circ\text{C}$. XRD and Raman spectroscopy were performed to evaluate the phase crystallization of LiCoO_2 film. Room temperature micro-Raman spectra was measured on a Jobin-Yvon T64000 spectrometer equipped with a liquid nitrogen charge-coupled device (CCD) detector, in a frequency range of $350\text{-}800\text{ cm}^{-1}$, using the 514.5 nm excitation line of an

Ar^+ laser, with an incident power of 1 mW in a $1\text{ }\mu\text{m}$ spot and in backscattering geometry. XRD were acquired using an X-ray Bruker, model D8 Discover, copper source of 40 kV and 40 mA, beam wavelength of 1.54 \AA and theta/2theta configuration, also called Bragg-Brentano configuration. Charge/discharge tests were performed in the flexible battery, after Ge deposition, and without breaking the chamber vacuum, to avoid reaction of battery with air, since no protection layers were deposited. The tests were performed with Gamry Reference 600TM potentiostat/galvanostat with the working electrode connected to Pt cathode current collector and the reference and counter electrode connected to anode current collector (Ti).

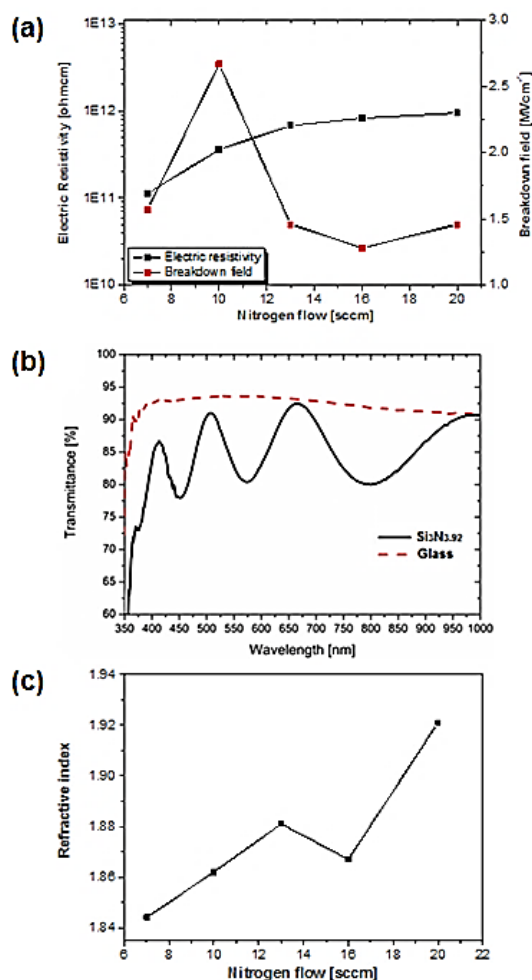


Fig. 2. (a) Electric resistivity and breakdown field results of Si_xN_y films as a function of nitrogen flow, (b) Transmission spectrum for the $\text{Si}_3\text{N}_{3.92}$ film (black line) and for the glass substrate (red dashed line) as function of wavelength, (c) Refractive index (measured at 650 nm) and calculated by the Swanepoel method [34] as function of nitrogen flow, during PVD deposition.

Results and discussion

In this work, the correlation between the selected materials and the electrochemical performance of the corresponding full battery is clearly presented. Silicon nitride (Si_xN_y) films is commonly applied in microelectronics systems, such as thin film transistors and

solar cells [35], due to their characteristics as a high diffusion barrier against water molecules and sodium ions [30], high thermal stability, elevated hardness, electrical resistivity and good dielectric properties [36]. In optics, it provides great transparency for the visible wavelengths [35]. Si_xN_y films are typically fabricated by chemical vapor deposition (CVD) processes [37]. However, in this work, this material was fabricated by RF magnetron sputtering, since we pretend to fabricate the entire battery by only PVD deposition techniques. Moreover, RF sputtering technique makes use of inert gases, lower temperatures (for bio and organic applications) and provide versatility and simplicity to change the parameters of film growth [38], as well as lower stressful stoichiometry [39], than the CVD processes. Here, Si_xN_y lithium barrier layer was evaluated recurring to chemical, electrical and optical measurements. The thickness and roughness of deposited films were measured in four points with the profilometer system (stylus has 12.5 μm of diameter and applies a force of 30 μN). The mean thickness of Si_xN_y films is 516.0 ± 58.7 nm with a roughness of 1.64 nm. Si_xN_y films composition was analyzed through EDS technique, and the films stoichiometry are indicated in **Table I**. Films stoichiometry was calculated fixing Si_3N_y and assuming the multiplicative factor to calculate the number of N atoms for 3 Si atoms, for each film. To measure the electric resistivity and breakdown field in Si_xN_y films, Al/ Si_xN_y /Al sandwiched structures was fabricated using the process previously described in Battery Materials section. **Fig. 2 (a)** displays the electric resistivity and breakdown field for RF-sputtered Si_xN_y films. The electrical resistivity, " ρ ", was calculated using the equation

$$\rho = \frac{V \times A}{I \times d} \quad (1)$$

where, " V " is the applied voltage, " I " is the measured current, A is the area of the metal contact and d the film thickness. As can be seen in **Fig. 2(a)**, the electrical

resistivity of Si_xN_y films increases with increased nitrogen flow, reaching the value of $9.51 \times 10^{11} \Omega\text{cm}$. For instance, our PVD- Si_xN_y film, deposited with 13 sccm of N_2 flow (reflecting in 65% of nitrogen ratio), show an electric resistivity value of $\sim 10^{11} \Omega\text{cm}$, which is in the same order of magnitude of the value obtained for CVD – Si_xN_y films fabricated at 100 $^\circ\text{C}$ and 250 $^\circ\text{C}$ [40]. Furthermore, M Vila, *et al.* [41] reported electric resistivity of $1 \times 10^{11} \Omega\text{cm}$ by RF sputtering (similar to our samples). Interestingly, the breakdown field value decreased with increased nitrogen flow. However, our PVD- Si_xN_y films can support higher electric field (up to 2.67 MVcm^{-1}) than with previous results of CVD- Si_xN_y films fabricated at 100 $^\circ\text{C}$ (up to 2 MVcm^{-1}) and 250 $^\circ\text{C}$ (up to $\sim 1 \text{ MVcm}^{-1}$) [40]. In order to improve the Si_xN_y thin-films characterization, optical transmittance measurements were also performed. An high quality transparent barrier coating could be interesting for single-film coatings and organic-inorganic stack but is also considerable interesting for food and pharmaceutical industry [42], [43]. The transmission spectrum of a typical $\text{Si}_3\text{N}_{3.92}$ film, deposited on glass substrate, is shown in **Fig. 2 (b)**. The transparency of the silicon nitride film is between 85 and 90%, between 400 and 1000 nm of wavelength range. The transmittance data of Si_xN_y films was used to calculate the film thickness and refractive index, by the Swanepoel method [34]. Calculated mean thickness was 518.0 nm, a very accurate result when compared with profilometer measurements (516.0 nm). Optical transmission as well as profilometer measurements were taken on the same pieces of the films. The refractive index of the RF-sputtered Si_xN_y films ranged from 1.84 to 1.92, at 650 nm of wavelength (**Fig. 2(c)**). The refractive index of the glass substrate was 1.52, considering a mean transmission of 91.8%. Due to reasonable combination of high electrical resistivity and breakdown field and taking in account a high quality transparent barrier coating, we incorporate the $\text{Si}_3\text{N}_{4.02}$ stoichiometric film as electrical insulator in our battery fabrication, considering flexible lithium battery

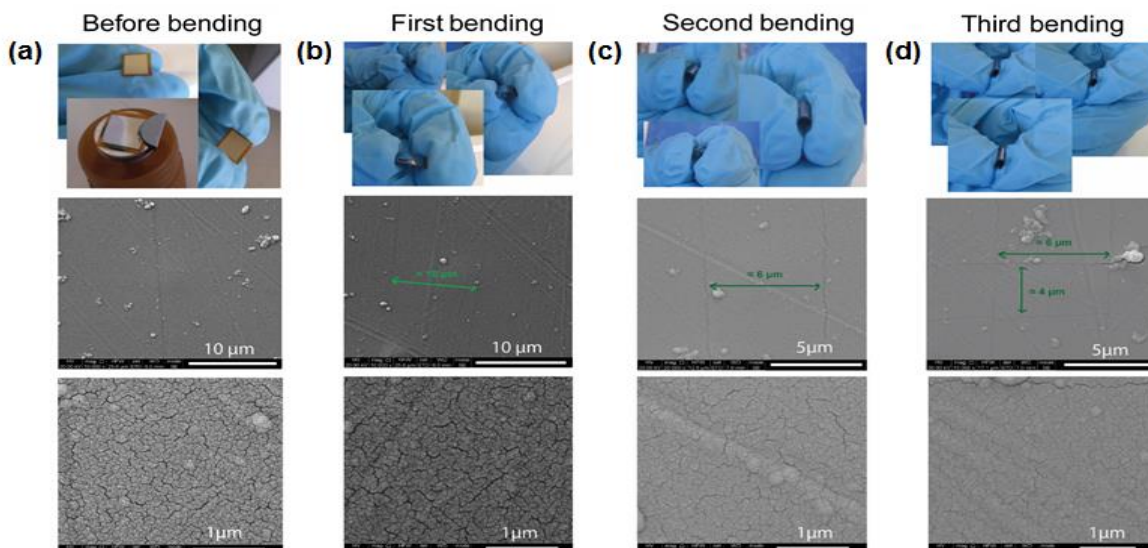


Fig. 3. Photos (top) and surface SEM images (below) with different magnification of kapton/ Si_3N_4 /Ti/Pt structure: (a) without bending, (b) after first bending, (c) after second bending, and (d) after third bending. Crack lines distance are indicated on SEM images.

applications.

Before the LiCoO₂ cathode deposition, it is important to evaluate the adhesion and stability properties of the multilayered structure (Kapton/Si₃N₄/Ti/Pt) which form the basis of the full-battery stack. For this purpose, electrical resistance and SEM measurements were performed after several bending experiments of the base structure. Electrical resistance was measured with a four-point system for more accurate measurements. **Fig. 3 (a)** presents the photos of the base structure without bending and the surface SEM acquisitions of Pt cathode current collector. A resistance of 1.4 Ω was measured. **Fig. 3 (b, c, d)** presents the same sample as before, but after the first, second and third bends. The bending process is shown on top photos. After the first bend (**Fig. 3 (b)**), it's visible on SEM images that some crack lines appeared on Pt surface spaced of ≈ 10 μm and all in the same direction. Despite crack lines, the sample remains similar to before bending, and the same resistance of 1.4 Ω was measured. After the second bending on the same direction (**Fig. 3 (c)**), SEM images of Pt surface show more crack lines than before, reducing the space between lines to ≈ 6 μm. A resistance of 1.5 Ω was measured. The third and final bend (**Fig. 3 (d)**) was on a perpendicular direction to previous bending's. Surface SEM images of Pt presented more crack lines in a perpendicular direction and spaced by ≈ 4 μm. A resistance between 4 and 20 Ω was measured, presenting a significant increase and variation on Pt thin-film resistance. Noteworthy that even after all the bends, the thin-films continued attached to the Kapton® substrate. The crystallization of LiCoO₂ films is one of the most challenging problems to improve thin film flexible microbatteries. LiCoO₂ usually needs an annealing around 700 °C for 1 hour to be completely crystalline [11], which is not compatible with most flexible substrates (e.g. kapton that supports until 400 °C). J. F. Whitacre *et al.* [44] reported a 150 nm thick LiCoO₂ film deposited on by RF-sputtering (RF power: 100 W; working pressure: 1.3 × 10⁻² mbar; Ar:O₂ = 3:1 to 1:1) and annealed at 300 °C, but with only a broad (104) peak observed by XRD analysis. In turn, Kumar *et al.* [45], that also deposited LiCoO₂ films on polyimide substrates by RF-sputtering (RF power: 50 to 150 W; working pressure: 3.0 × 10⁻³ mbar; O₂: Ar = 1:9), reported an increase of orientation in (104) plane with the increase of RF power. Group of S.W. Song [46] performed Raman spectroscopic characterizations of the annealed (520 °C) RF-sputtered LiCoO₂ films (power density: 3.53 W/cm²; Ar working pressure: 1.3 × 10⁻² mbar) revealing the presence of the HT-LiCoO₂ and LT-LiCoO₂ phases after performing several cycling tests. Another study demonstrated that HT-LiCoO₂ films can be created in the narrow substrate temperature range of 250 – 300 °C using pulsed laser deposition technique (KrF excimer laser (λ = 248 nm); Energy density: 1.8 J.cm⁻²; O₂ pressure: 1.3 × 10⁻³ mbar). For substrate temperatures, higher than 350 °C, HT-LiCoO₂ coexist with Co₂O₃, Co₃O₄ and LiCoO₄ impurities [47].

In this work, an annealing at 400 °C was performed in the kapton/Si₃N₄/Ti/Pt/LiCoO₂ structure. LiCoO₂

crystallization and morphology were characterized by XRD, Raman and SEM techniques. XRD pattern and Raman spectrum for the annealed LiCoO₂ sample (at 400 °C in air conditions) are shown on the **Fig. 4(a)**. The two red dashed lines corresponds to the two main planes on HT-LiCoO₂ phase, the (101) and (104) planes. It can be seen that the plane (101) prevails relatively to the (104) plane. Thus, in what follows, the annealed LiCoO₂ will be considered for battery fabrication. The other peaks in the XRD pattern are related with previous films (mainly Pt). The results obtained by XRD are essentially confirmed by the Raman investigation reported on inset of **Fig. 4(a)**. HT-LiCoO₂ hexagonal phase is observed with two typical phonon modes at 486 and 596 cm⁻¹ [8], [48] in annealed LiCoO₂ film. We also found one extra peak around 660 cm⁻¹ that can probably be linked to an undesirable oxide phase or a nanosize effect [49].

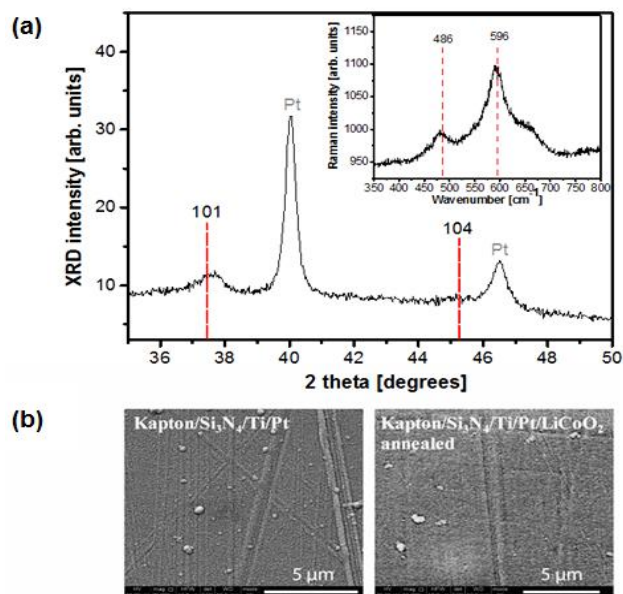


Fig. 4. (a) XRD pattern and corresponding Raman spectrum (on inset) of LiCoO₂ film deposited on Kapton® substrate and annealed at 400 °C in air. The two vertical red dashed lines correspond to main peaks (XRD) and vibrational modes (Raman) predict in the hexagonal R3m phase of LiCoO₂. (b) Surface SEM pictures (5 μm of magnification) of structure before LiCoO₂ deposition (left) and after LiCoO₂ deposition and annealed at 400 °C in air (right).

SEM images (**Fig. 4 (b)**) were acquired to compare the surface morphology of the films deposited on Kapton® substrate during sample preparation: (i) before LiCoO₂ deposition (Si₃N₄/Ti/Pt) and (ii) after LiCoO₂ deposition and annealed at 400 °C in air conditions (Si₃N₄/Ti/Pt/LiCoO₂ annealed). Both structures have a smoother surface. These evaluations are important in order to fabricate high capacity flexible microbatteries, since the structure and morphology of the cathode greatly affects the battery performance and adhesion/stability of the upper films.

For Li battery applications, the electrolyte should reveal a negligible electronic conductivity and high ionic conductivity. Therefore, the electric resistivity and

breakdown field properties of LiPON film were evaluated. The measurements were performed at room temperature and atmospheric conditions. In two-dimensional (2D) thin-film lithium battery exist some regions that are more vulnerable to short circuits phenomena, due to the low electrolyte thickness which may not be sufficient to electrically isolate the electrode materials. This problematic zone is represented in Fig. 1 by a black circle and was strengthened with Si₃N₄ and LiPO thin-films to increase electrical insulation between the electrodes. Therefore, the electrical measurements were performed in LiPON films less than 1 μm thick. Specifically, in our work, the electric resistivity (ρ) and breakdown field (BE) properties were evaluated for 600 nm thick LiPON films. A DC constant potential (between 0 to 10 V) was applied through the MIM structure described in Battery Materials section, causing the flow of an electronic current. The two properties could be obtained through the relationship between the emission current density (J) and the electric field (E) applied to RF sputtered LiPON film, which is shown in Fig. 5 (a). Our experimental results show that the LiPON film can support high voltages up to 5.6 V (E = 1 × 10⁵ V/cm), which suits for practical applications powered by 4 V cell Li batteries. Above these voltage, the flow current is very high and damage the film. Moreover, a moderate electric resistivity of 4 × 10⁸ Ωcm was measured for our 600 nm thick LiPON films. This value was extracted with 1 V applied to the film and using the equation 1. The morphology of the film can affect seriously the electrical properties. Particularly, our LiPON film shows a rough surface with large sized particles (see the SEM image inset in Fig. 5 (a)). The existence of a rough surface could justify the low electric resistivity value. Moreover, the significant difference related to the theoretical value of ~10¹⁴ Ωcm could be attributed to the fact that the measurements were done in air which can lead to the contamination of the surface, and the interface quality of the metal/electrolyte [50]. The electrolyte electrical resistivity is a critical point to be considered, since could compromise all battery design (high battery self-discharge could occur), even when the all battery materials show the best structure and composition properties, and high capacities [51].

Optimization of electric and ionic conductivities of LiPON electrolyte has been reported in the last years. Y. Su *et al.* [14] reported 1330 nm thick RF-sputtered LiPON films (RF power: 100 W; N₂ pressure: 1.5 × 10⁻³ mbar; stoichiometry: Li_{3.13}PO_{1.69}N_{1.39}) with an ionic conductivity of 4.9 × 10⁻⁶ S/cm (at 22 °C) and an electronic conductivity of 1.6 × 10⁻¹² S/cm (by current – time curves at a constant voltage). Furthermore, S. Nowak *et al.* [50] show that 195 nm thick LiPON films fabricated by ion-beam sputtering (RF power: 130 W; Beam energy: 700 eV; current density: 0.6 mA/cm²) reveals an ionic conductivity of 1-2 × 10⁻⁷ S/cm (at 25 °C) with an electronic conductivity around 10⁻¹¹ S/cm. More recently 15 nm thick LiPON layers (RF power: 225 W; N₂ flow: 30 sccm; stoichiometry: Li_{2.14}PO_{1.85}N_{0.91}) with an ionic conductivity of 1 × 10⁻⁶ S/cm (at 27 °C) and high

electrical resistivity of ~10¹⁵ Ω.cm) were also demonstrated by the work of B. Put *et al.* [52]. LiPON findings needs to be correlated to battery functionality, because when the electrolyte is significantly downscaled to only few nanometers in size, the chemical stability and the ability of the electrolyte to prevent electronic current flow, between the active electrodes and over the cycles could be compromised [51].

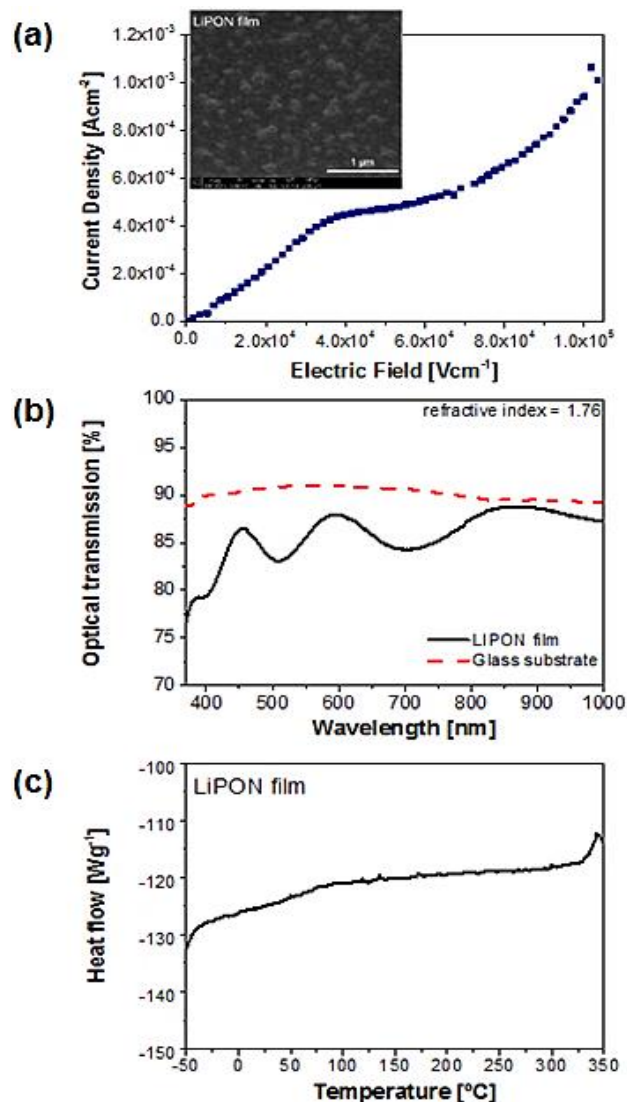


Fig. 5. (a) Typical J – E profile for LiPON film fabricated at 6 × 10⁻³ mbar of Ar pressure. Inset: surface SEM image of LiPON film. Optical transmission spectra, (b) and DSC curve, (c) for the LiPON film fabricated at 6 × 10⁻³ mbar of Ar pressure. The transmission of a raw glass substrate is shown as red dash-dotted line in (b).

The ionic conductivity measurements on LiPON films were also performed by our group, through electrochemical impedance spectroscopy (EIS), showing values in range of 10⁻⁷ – 10⁻⁶ Scm⁻¹, for temperatures between 22 °C and 43 °C [53]. Pt (contacts)/LiPON/Pt (contacts) sandwich structures deposited on aluminum substrates were used to perform the EIS. Pt was used to avoid possible reactions at Al/LiPON interfaces. The experiments were carried out in an Ar glovebox (O₂, H₂O < 1 ppm) by applying an AC voltage of 12.5 mV within a

frequency range from 65 kHz to 0.5 Hz (Autolab PGSTAT – 12 (Eco Chemie) set-up) at different controlled temperatures (Büchi TO-50) [53].

Fig. 5 (b) shows the optical transmission of LiPON film. A high transparency between 75 and 90% for 350 to 1000 nm is observed, which could be interesting for transparent electronic devices [54]. Similar for Si_xN_y films, the transmittance data were used to calculate the film thickness (a mean thickness of 548 nm) and refractive index of 1.76, by the Swanepoel method [34]. The film thickness is a very accurate value when compared with profilometer measurement (555 nm). Optical transmission as well as profilometer measurements were taken on the same pieces of the LiPON film. The refractive index of the glass substrate, in which LiPON was deposited, was 1.61, considering a transmission of 89.7%.

RF-sputtered LiPON films (RF power: 100 W; N_2 pressure: 1.5×10^{-3} mbar) with thickness range from 200 to 2000 nm and a transparency higher than 80% (refractive index of 1.8) were also reported by Y. Su *et al.* [14]. Furthermore, X. Yu *et al.* [55] reports LiPON films deposited by RF sputtering (RF power: 100 W; $\text{Ar}:\text{O}_2 = 3:2$) with an refractive index between 1.7 and 1.9.

LiPON electrolyte should be also thermally stable, in order to promote a good battery performance over a wide temperature range. Here, DSC technique was applied to investigate the thermal behavior of the LiPON films. The DSC results in **Fig. 5 (c)** show that the LiPON film is stable when subjected to temperatures up to 300 °C. However, a possible chemical change in LiPON film is observed at a temperature close to 350 °C. No visual changes were observed in the LiPON. Among this observation, we considered the fabricated LiPON electrolyte film for the battery fabrication, since it holds a temperature range of -50 °C to 300 °C, without thermal events.

After structural, chemical, optical, thermal, electrical and electrochemical evaluations of the battery elements, a full Li-ion battery was fabricated, using the same deposition conditions used for each material and using the Ge as thin-film anode. The full-battery was also fabricated on silicon substrate for microstructure investigation by SEM technique. Si substrate facilitate the cross-section visualization of the battery. A well-organized multilayered-structure of the main components of the battery (cathode/electrolyte/anode), with smooth interfaces and good adhesion layers are observed in SEM picture (**Fig. 6**). Measured thickness of each layer is also present in figure 6. The thickness measured by SEM is equivalent (error < 5%) to the thickness measured by the microbalance during deposition. However, the thickness of LiPON film appears significantly thinner than expected (~1 μm thick) which could be justified with acoustic properties settled in microbalance system.

The charge/discharge tests in the full battery were performed to evaluate the electrochemical behavior. The voltage profiles of the battery during discharge cycles in the region of 0 – 2 V at current of 100 and 200 nA are shown in **Fig. 7 (a)**. Potentiostatic charges of 4.1 V during

60 min were applied to the Ge-LiCoO₂ battery. The expected voltage of 4.1 V was not reached. After the first discharge cycle, a capacity of 46 nAhcm⁻² was calculated.

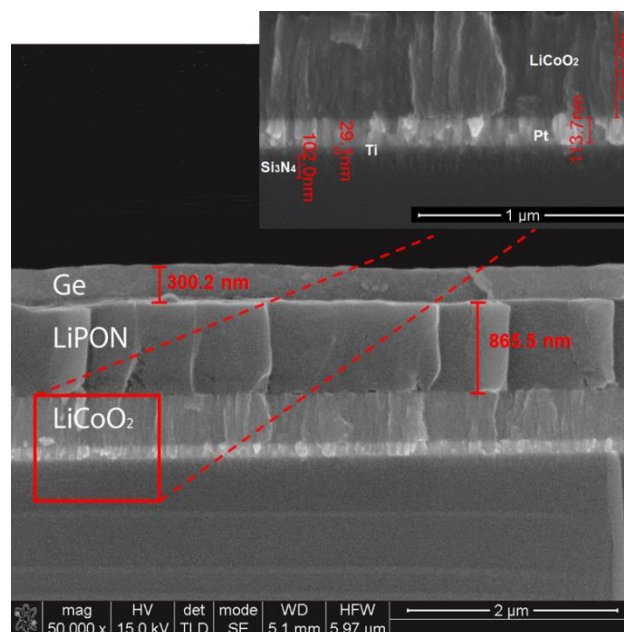


Fig. 6. SEM image (cross-section) of the Li-ion battery with Ge as anode, before the battery tests. The substrate is silicon.

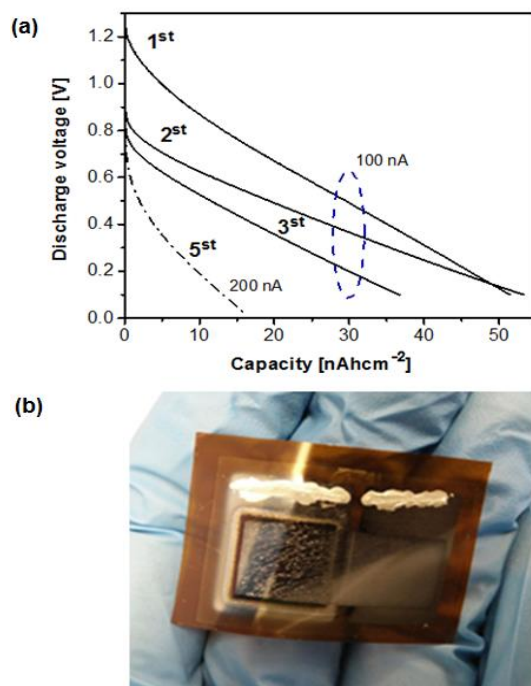


Fig. 7. (a) Discharge properties of the flexible thin-film Li-ion battery during 5 charge/discharge cycles, (b) Photograph of the battery.

However, this capacity reduces rapidly in the next cycles, as can be calculated from discharge data. A theoretical capacity of 69 μAhcm^{-2} for LiCoO₂ can be expected. Our battery has only 13% coulombic efficiency in the 1th cycle and decrease in the next cycles. This low capacity could be justified by many factors: (i) lack of Li ion in

electrolyte film; (ii) oxygen defects in LiCoO₂ that consumes Li ions; low electric resistivity and bad morphology structure of LiPON electrolyte, inefficient electrical insulator barrier at the problematic battery zone (see Fig. 1); and/or Li ions ends up in the build-up of SEI interface during the insertion and extraction mechanisms during the electrochemical battery operation, making Ge not really charged. A battery picture is also shown in Fig. 7 (b). Battery is already destroyed in this picture, since it was obtained after several charge/discharge cycles and after exposing battery to atmospheric conditions. Despite the bad capacity retention observed, the aim of this work is highlight the simplified, low-cost and micro-electromechanical systems (MEMS) technology compatibility of a flexible solid-state Li-ion fabrication. These findings put in evidence the strongly lithium battery dependence of the properties of all battery elements [56, 57].

Conclusion

Cathode and electrolyte properties, such as, structure, composition, thermal, optical and electric resistivity were investigated and correlated with the electrochemical potential of the full Li-ion battery. RF-sputtered LiCoO₂ cathode (with 120 W of RF power; 6 x 10⁻³ mbar of pressure and 17/3 sccm of Ar/O₂ gases) shows the preferable HT-LiCoO₂ phase with (101) plane by an annealing at only 400 °C, which is compatible with flexible plastic/polymeric substrates. A moderate electrical resistivity of 10⁸ Ωcm of LiPON film was achieved. Moreover, no thermal reactions up to 300 °C were observed for high transparent rf-sputtered LiPON film (DSC and optical transmission investigations). The adhesion and stability of the films were evaluated by SEM and resistance measurements after simple bending tests. Although it was observed a variation on Pt resistance after three bending experiments, the multilayer base structure (Si₃N₄/Ti/Pt) continued attached to the Kapton® substrate without visible changes. The RF-sputtered Si₃N₄ lithium shows an electric resistivity of 9.51 × 10¹¹ Ωcm and a mean breakdown field of 1.69 MVcm⁻¹. Refractive indexes could be reached among 1.921 and 1.844 at 650 nm by simple adjustment of nitrogen ratio. These findings led to the fabrication of a flexible solid-state Li-ion battery recurring only to PVD techniques. A 127 μm thick plastic Kapton® was used as substrate to provide flexibility to the battery. A well-organized battery structure was observed by cross-section SEM images. Despite the observed low initial capacity (46 nAhcm⁻²) and retention fading along charge/discharge cycles, a solid-state battery was developed using materials and techniques compatible with those used in MEMS industry.

Acknowledgements

This work is supported by FCT with the reference project UID/EEA/04436/2013, by FEDER funds through the COMPETE 2020 – Programa Operacional Competitividade e Internacionalização (POCI) with the reference project POCI-01-0145-FEDER-006941, and by the strategic projects UID/FIS/04650/2013 and PEST – C/QUI/UI0686/2013. EMFV

is grateful for financial support through the FCT grant SFRH/BPD/95905/2013.

Author's contributions

Conceived the plan: E.M.F. Vieira, J. F. Ribeiro and L.M. Gonçalves; Performed the experiments: E.M.F. Vieira, J. F. Ribeiro, R. Sousa; A. G. Rolo and M. M. Silva; Data analysis: E. M. F. Vieira, J. F. Ribeiro, R. Sousa; A. G. Rolo, M. M. Silva and L. M. Gonçalves; Wrote the paper: E. M. F. Vieira. Authors have no competing financial interests.

References

1. Diouf, B.; Pode, R; *Renew. Energy*, **2015**, *76*, 375. DOI: [10.1016/j.renene.2014.11.058](https://doi.org/10.1016/j.renene.2014.11.058)
2. Nagai, H.; Suzuki, T.; Takahashi, Y.; Sato, M; *Funct. Mater. Lett.*, **2016**, *9*, 1650046. DOI: [10.1142/S1793604716500466](https://doi.org/10.1142/S1793604716500466)
3. Khan, Y.; Ostfeld, A. E.; Lochner, C. M.; Pierre, A.; Arias, A. C; *Adv. Mater.*, **2016**, *28*, 4373. DOI: [10.1002/adma.201504366](https://doi.org/10.1002/adma.201504366)
4. Wang, C.-M; *J. Mater. Res.*, **2015**, *30*, 326. DOI: [10.1557/jmr.2014.281](https://doi.org/10.1557/jmr.2014.281)
5. Khanna, V. K; *J. Phys. D. Appl. Phys.*, **2011**, *44*, 034004. DOI: [10.1088/0022-3727/44/3/034004](https://doi.org/10.1088/0022-3727/44/3/034004)
6. Pasquier, A. Du; Plitz I.; Menocal, S.; Amatucci, G; *J. Power Sources*, **2003**, *115*, 171. DOI: [10.1016/S0378-7753\(02\)00718-8](https://doi.org/10.1016/S0378-7753(02)00718-8)
7. Xu, J.; Dou, S.; Liu, H.; Dai, L; *Nano Energy*, **2013**, *2*, 439. DOI: [10.1016/j.nanoen.2013.05.013](https://doi.org/10.1016/j.nanoen.2013.05.013)
8. Inaba, M.; Iriyama, Y.; Ogumi, Z.; Todzuka, Y.; Tasaka, A; *J. Raman Spectrosc.*, **1997**, *28*, 613. DOI: [10.1002/\(SICI\)1097-4555\(199708\)28:8<613::AID-JRS138>3.0.CO;2-T](https://doi.org/10.1002/(SICI)1097-4555(199708)28:8<613::AID-JRS138>3.0.CO;2-T)
9. Liao, C.-L.; Fung, K.-Z; *J. Power Sources*, **2004**, *128*, 263. DOI: [10.1016/j.jpowsour.2003.09.065](https://doi.org/10.1016/j.jpowsour.2003.09.065)
10. Kumar, P. J.; Babu, K. J.; Hussain, O. M.; Garg, A. B.; Mittal, R.; Mukhopadhyay, R; *Solid State Physics*, 55th DAE Solid State Phys. Symp. Proc. 2010 AIP Conf. Proc. *1349*, 381-382, **2011**.
11. Bates, J. B.; Dudney, N. J.; Neudecker, B. J.; Hart, F. X.; Jun, H. P.; Hackney, S. A; *J. Electrochem. Soc.*, **2000**, *147*, 59. DOI: [10.1149/1.1393157](https://doi.org/10.1149/1.1393157)
12. Bates, J. B.; Dudney, N. J.; Gruzalski, G. R.; Zuhr, R. A.; Choudhury, A.; Luck, C. F.; Robertson, J. D; *J. Power Sources*, **1993**, *43*, 103. DOI: [10.1016/0378-7753\(93\)80106-Y](https://doi.org/10.1016/0378-7753(93)80106-Y)
13. Nisula, M.; Shindo, Y.; Koga, H.; Karppinen, M; *Chem. Mater.*, **2015**, *27*, 6987. DOI: [10.1021/acs.chemmater.5b02199](https://doi.org/10.1021/acs.chemmater.5b02199)
14. Su, Y.; Falgenhauer, J.; Polity, A.; Leichtweiß, T.; Kronenberger, A.; Obel, J.; Zhou, S.; Schlettwein, D.; Janek, J.; Meyer, B. K.; *Solid State Ionics*, **2015**, *282*, 63. DOI: [10.1016/j.ssi.2015.09.022](https://doi.org/10.1016/j.ssi.2015.09.022)
15. Song, J.; Yang, X.; Zeng, S.-S.; Cai, M.-Z.; Zhang, L.-T.; Dong, Q.-F.; Zheng, M.-S.; Wu, S.-T.; Wu, Q.-H; *J. Micromechanics Microengineering*, **2009**, *19*, 045004. DOI: [10.1088/0960-1317/19/4/045004](https://doi.org/10.1088/0960-1317/19/4/045004)
16. Oleshko, V. P.; Lam, T.; Ruzmetov, D.; Haney, P.; Lezec, H. J.; Davydov, A. V.; Krylyuk, S.; Cumings, J.; Talin, A. A; *Nanoscale*, **2014**, *6*, 11756. DOI: [10.1039/c4nr01666a](https://doi.org/10.1039/c4nr01666a)
17. Christiansen, A. S.; Stamate, E.; Thydén, K.; Younesi, R.; Holtappels, P; *J. Power Sources*, **2015**, *273*, 863. DOI: [10.1016/j.jpowsour.2014.09.174](https://doi.org/10.1016/j.jpowsour.2014.09.174)
18. Dudney, N. J; *Mater. Sci. Eng. B*, **2005**, *116*, 245. DOI: [10.1016/j.mseb.2004.05.045](https://doi.org/10.1016/j.mseb.2004.05.045)
19. Nitta, N.; Wu, F.; Lee, J. T.; Yushin, G; *Mater. Today*, **2015**, *18*, 252. DOI: [10.1016/j.mattod.2014.10.040](https://doi.org/10.1016/j.mattod.2014.10.040)
20. Lim, L. Y.; Liu, N.; Cui, Y.; Toney, M. F; *Chem. Mater.*, **2014**, *26*, 3739. DOI: [10.1021/cm501233k](https://doi.org/10.1021/cm501233k)
21. Li, X.; Yang, Z.; Fu, Y.; Qiao, L.; Li, D.; Yue, H.; He, D; *ACS Nano*, **2015**, *9*, 1858.

- DOI: [10.1021/nn506760p](https://doi.org/10.1021/nn506760p)
22. Cui, G.; Gu, L.; Zhi, L.; Kaskhedikar, N.; Aken, P. A. van; Müllen, K.; Maier, J; *Adv. Mater.*, **2008**, *20*, 3079.
DOI: [10.1002/adma.200800586](https://doi.org/10.1002/adma.200800586)
23. Gwon, H.; Hong, J.; Kim, H.; Seo, D.-H.; Jeon, S.; Kang, K.; *Energy Environ. Sci.* **2014**, *7*, 538.
DOI: [10.1039/C3EE42927J](https://doi.org/10.1039/C3EE42927J)
24. Fang, S.; Shen, L.; Zheng, H.; Zhang, X; *J. Mater. Chem. A* **2015**, *3*, 1498.
DOI: [10.1039/C4TA04350B](https://doi.org/10.1039/C4TA04350B)
25. Palanisamy, K.; Um, J. H.; Jeong, M.; Yoon, W.-S; *Sci. Rep.* **2016**, *6*, 31275.
DOI: [10.1038/srep31275](https://doi.org/10.1038/srep31275)
26. Wang, X.; Lu, X.; Liu, B.; Chen, D.; Tong, Y.; Shen, G; *Adv. Mater.* **2014**, *26*, 4763.
DOI: [10.1002/adma.201400910](https://doi.org/10.1002/adma.201400910)
27. Tarascon, J.-M.; Armand, M.; *Nature*, **2001**, *414*, 359.
DOI: [10.1038/35104644](https://doi.org/10.1038/35104644)
28. Dupont, "Kapton® datasheet," 2015.
29. Francioso, L.; Pascali, C. De; Farella, I.; Martucci, C.; Cretì, P.; Siciliano, P.; Perrone, A; *J. Power Sources*, **2011**, *196*, 3239.
DOI: [10.1016/j.jpowsour.2010.11.081](https://doi.org/10.1016/j.jpowsour.2010.11.081)
30. Pernice, W. H. P.; Li, M.; Gallagher, D. F. G.; Tang, H. X; *J. Opt. A Pure Appl. Opt.*, **2009**, *11*, 114017.
DOI: [10.1088/1464-4258/11/11/114017](https://doi.org/10.1088/1464-4258/11/11/114017)
31. Ribeiro, J. F.; Sousa, R.; Cunha, D. J.; Vieira, E. M. F.; Silva, M. M.; Dupont, L.; Goncalves, L. M; *J. Phys. D: Appl. Phys.*, **2015**, *48*, 395306.
DOI: [10.1088/0022-3727/48/39/395306](https://doi.org/10.1088/0022-3727/48/39/395306)
32. Johnson, L. G; U.S. Patent 6,242,129 B1, **2001**.
33. Kobayashi, N.; Kawakami, S.; Yamamoto, T; U.S. Patent 6,517,974 B1, **2003**.
34. Swanepoel, R.; *J. Phys. E.*, **1983**, *16*, 1214.
DOI: [10.1088/0022-3735/16/12/023](https://doi.org/10.1088/0022-3735/16/12/023)
35. Verlaan, V.; Bakker, R.; Werf, C. H. M. van der; Houweling, Z. S.; Mai, Y.; Rath, J. K.; Schropp, R. E. I; *Surf. Coatings Technol.*, **2007**, *201*, 9285.
DOI: [10.1016/j.surfcoat.2007.03.057](https://doi.org/10.1016/j.surfcoat.2007.03.057)
36. Schmidt, H.; Gruber, W.; Borchardt, G.; Bruns, M.; Rudolphi, M.; Baumann, H; *Thin Solid Films*, **2004**, *450*, 346.
DOI: [10.1016/j.tsf.2003.11.274](https://doi.org/10.1016/j.tsf.2003.11.274)
37. Habraken F. H. P. M.; Kuiper, A. E. T.; *Mater. Sci. Eng. R Reports*, **1994**, *12*, 123.
DOI: [10.1016/0927-796X\(94\)90006-X](https://doi.org/10.1016/0927-796X(94)90006-X)
38. Signore, M. A.; Sytchkova, A.; Dimaio, D.; Cappello, A.; Rizzo, A; *Opt. Mater. (Amst.)*, **2012**, *34*, 632.
DOI: [10.1016/j.optmat.2011.09.012](https://doi.org/10.1016/j.optmat.2011.09.012)
39. Mousinho, A. P.; Mansano, R. D.; Zambom, L. S.; Passaro, A; *J. Phys. Conf. Ser.*, **2012**, *370*, 012015.
DOI: [10.1088/1742-6596/370/1/012015](https://doi.org/10.1088/1742-6596/370/1/012015)
40. Alpuim, P.; Gonçalves, L. M.; Marins, E. S.; Viseu, T. M. R.; Ferdov, S.; Bourée, J. E; *Thin Solid Films*, **2009**, *517*, 3503.
DOI: [10.1016/j.tsf.2009.01.077](https://doi.org/10.1016/j.tsf.2009.01.077)
41. Vila, M.; Prieto, C.; Ramirez, R; *Thin Solid Films*, **2004**, *459*, 195.
DOI: [10.1016/j.tsf.2003.12.082](https://doi.org/10.1016/j.tsf.2003.12.082)
42. Chen, T. N.; Wu, D. S.; Wu, C. C.; Chiang, C. C.; Lin, H. B.; Chen, Y. P.; Horng, R. H; *Thin Solid Films*, **2006**, *514*, 188.
DOI: [10.1016/j.tsf.2006.02.039](https://doi.org/10.1016/j.tsf.2006.02.039)
43. Wu, D.-S.; Chen, T.-N.; Wu, C.-C.; Chiang, C.-C.; Chen, Y.-P.; Horng, R.-H.; Juang, F.-S; *Chem. Vap. Depos.*, **2006**, *12*, 220.
DOI: [10.1002/cvde.200506436](https://doi.org/10.1002/cvde.200506436)
44. Whitacre, J. F.; West, W. C.; Brandon, E.; Ratnakumar, B. V; *J. Electrochem. Soc.* **2001**, *148*, A1078.
DOI: [10.1149/1.1400119](https://doi.org/10.1149/1.1400119)
45. Kumar, P. J.; Babu, K. J.; Hussain, O. M; *Adv. Sci. Eng. Med.* **2012**, *4*, 190.
DOI: [10.1166/asem.2012.1147](https://doi.org/10.1166/asem.2012.1147)
46. Song, S.-W.; Hong, S.-J.; Park, H. Y.; Lim, Y. C.; Lee, K. C; *Electrochem. Solid-State Lett.* **2009**, *12*, A159.
DOI: [10.1149/1.3139530](https://doi.org/10.1149/1.3139530)
47. Tsuruhama, T.; Hitosugi, T.; Oki, H.; Hirose, Y.; Hasegawa, T; *Appl. Phys. Express* **2009**, *2*, 085502.
DOI: [10.1143/APEX.2.085502](https://doi.org/10.1143/APEX.2.085502)
48. Pan, H.; Yang, Y; *J. Power Sources*, **2009**, *189*, 633.
DOI: [10.1016/j.jpowsour.2008.09.065](https://doi.org/10.1016/j.jpowsour.2008.09.065)
49. Sivajee Ganesh K.; Purusottam Reddy, B.; Jeevan Kumar, P.; Jayanthbabu, K.; Rosaiah, P.; Hussain, O. M; *J. Solid. State Electrochem.*, **2015**, *19*, 3621.
DOI: [10.1007/s10008-015-2963-z](https://doi.org/10.1007/s10008-015-2963-z)
50. Nowak, S.; Berkemeier, F.; Schmitz, G; *J. Power Sources*, **2015**, *275*, 144.
DOI: [10.1016/j.jpowsour.2014.10.202](https://doi.org/10.1016/j.jpowsour.2014.10.202)
51. Ruzmetov, D.; Oleshko, V. P.; Haney, P. M.; Lezec, H. J.; Karki, K.; Baloch, K. H.; Agrawal, A. K.; Davydov, A. V.; Krylyuk, S.; Liu, Y.; Huang, J.; Tanase, M.; Cumings, J.; Talin, A. A; *Nano Lett.*, **2012**, *12*, 505.
DOI: [10.1021/nl204047z](https://doi.org/10.1021/nl204047z)
52. Put, B.; Vereecken, P. M.; Meererschaut, J.; Sepúlveda, A.; Stesmans, A; *ACS Appl. Mater. Interfaces* **2016**, *8*, 7060.
DOI: [10.1021/acsami.5b12500](https://doi.org/10.1021/acsami.5b12500)
53. Ribeiro, J. F.; Sousa, R.; Carmo, J. P.; Gonçalves, L. M.; Silva, M. F.; Silva, M. M.; Correia, J. H; *Thin Solid Films*, **2012**, *522*, 85.
DOI: [10.1016/j.tsf.2012.09.007](https://doi.org/10.1016/j.tsf.2012.09.007)
54. Pat, S.; Özen, S.; Şenay, V.; Korkmaz, Ş; *Scanning*, **2016**, *38*, 317.
DOI: [10.1002/sca.21272](https://doi.org/10.1002/sca.21272)
55. Yu, X.; *J. Electrochem. Soc.* **1997**, *144*, 524.
DOI: [10.1149/1.1837443](https://doi.org/10.1149/1.1837443)
56. Deng, D; *Energy Sci. Eng.* **2015**, *3*, 385.
DOI: [10.1002/ese3.95](https://doi.org/10.1002/ese3.95)
57. Khan, Y.; Ostfeld, A. E.; Lochner, C. M.; Pierre, A.; Arias, A. C; *Adv. Mater.* **2016**, *28*, 4373.
DOI: [10.1002/adma.201504366](https://doi.org/10.1002/adma.201504366)